

Flux calibration of the AAO/UKST SuperCOSMOS $H\alpha$ Survey

David J. Frew^{1,2*}, Ivan S. Bojčić^{1,2,3}, Quentin A. Parker^{1,2,3}, Mark J. Pierce^{1,4},
M.L.P. Gunawardhana⁵ and W.A. Reid^{1,2}

¹ *Department of Physics and Astronomy, Macquarie University, Sydney, NSW 2109 Australia*

² *Research Centre for Astronomy, Astrophysics and Astrophotonics, Macquarie University, Sydney, NSW 2109 Australia*

³ *Australian Astronomical Observatory, PO Box 915, North Ryde, NSW 1670, Australia*

⁴ *Department of Physics, University of Bristol, Bristol, BS8 1TL, UK*

⁵ *Sydney Institute for Astronomy, School of Physics, The University of Sydney, NSW 2006, Australia*

Accepted . Received ; in original form

ABSTRACT

The AAO/UKST SuperCOSMOS $H\alpha$ Survey (SHS) of the southern Galactic plane was, when completed in 2003, a powerful new addition to wide-field surveys. It has a combination of areal coverage, spatial resolution and flux sensitivity in a narrow imaging band which still marks it out today as an excellent resource for the astronomical community. The 233 separate fields are available online in digital form, with each field covering 25 square degrees. The SHS has been the motivation for equivalent surveys in the north, and new digital $H\alpha$ surveys now beginning in the south such as VPHAS+. The SHS has been the foundation of many important follow-up discovery projects in the southern sky with the Macquarie/AAO/Strasbourg $H\alpha$ (MASH) planetary nebula project being a particularly successful example. However, the full astrophysical potential of the SHS has been hampered by lack of a clear route to acceptable flux calibration from the base photographic data. We have determined the flux calibration factors for 170 separate SHS fields, and present a direct pathway to the measurement of integrated $H\alpha$ fluxes and surface brightnesses for resolved nebulae detected in the SHS. We also include a catalogue of integrated $H\alpha$ fluxes for 88 known PNe, and several HII regions and other objects measured from the SHS, and use these data to show that integrated fluxes, accurate to $\pm 0.1 - 0.15$ dex, can be generally obtained across these survey fields. For the remaining 63 fields, a mean calibration factor of 12.0 counts/px/rayleigh can be used, which will allow the determination of reasonable integrated fluxes accurate to better than ± 0.2 dex. We outline the procedures involved and the problems and limitations that need to be appreciated in achieving such flux measurements. This paper forms a handy reference source that will significantly increase the scientific utility of the SHS.

Key words: astronomical databases: surveys; techniques: photometric; ISM: general, planetary nebulae; HII regions; supernova remnants

1 INTRODUCTION

The AAO/UKST SuperCOSMOS $H\alpha$ Survey (SHS; Parker et al. 2005, hereafter Paper I) provides high-resolution ($\sim 1''$), narrow-band, digital imaging data of the Southern Galactic Plane (SGP). The excellent combination of survey characteristics has made the SHS a powerful tool for the detection of extended, low surface brightness emission nebulosity over a range of angular scales from arcseconds to degrees (refer to later references). The SHS is also sensitive to faint point source $H\alpha$ emitters such as WR stars, Be and B[e] stars, T Tauri stars, symbiotic stars, cataclysmic variables,

and other exotica (Drew et al. 2003; Hopewell et al. 2005; Pretorius & Knigge 2008).

The survey utilised the 1.2-m UK Schmidt Telescope (UKST) at Siding Spring Observatory between 1998 and 2003. Exposures were taken through a high specification, monolithic $H\alpha$ interference filter with a clear aperture of approximately 305 mm, a central wavelength of 6590Å, a peak transmission of $\sim 90\%$ and a full width at half maximum (FWHM) of 70Å (Parker & Bland-Hawthorn 1998). This was sufficient to cover the $H\alpha$ and both [N II] $\lambda\lambda 6548, 84$ Å emission lines across the full range of radial velocity observed for Galactic emission (± 300 km s $^{-1}$).

The SHS footprint covers about 4000 square degrees of the SGP between $l = 210^\circ - 30^\circ$, and to a latitude, $|b| \approx 10 - 13^\circ$. It comprises 233 distinct but overlapping 5° survey exposures on non-standard field centres 4° apart (cf. the normal 5° -degree spacing),

* E-mail: david.frew@mq.edu.au

together with 40 fields covering a separate contiguous region of 650 square degrees in and around the Magellanic Clouds (Morgan, Parker & Philipps 1999). Each survey field consisted of a 3-hour $H\alpha$ Tech-Pan exposure and a matching, usually contemporaneous, 15-min broad-band (5900–6900Å) ‘short-red’ (SR) exposure taken with an OG590 filter¹ for continuum subtraction purposes. To date the SHS is the only high-resolution $H\alpha$ survey covering the full SGP. Earlier work by J. Meaburn and co-workers used a square multi-element interference filter on the UKST, with a FWHM of 105Å when used in combination with the 098-04 emulsion (Elliott & Meaburn 1976), but the plates only covered limited areas of the SGP (e.g. Elliott, Goudis & Meaburn 1976; Davies et al. 1978; Meaburn & White 1982). However, the coverage of the Magellanic Clouds was relatively complete (Davies, Elliott & Meaburn 1976; Goudis & Meaburn 1978; Meaburn 1980). However these survey plates are not generally available to the community.

The scanned SHS data at $10\mu\text{m}$ ($0.67''$) resolution is available online in digital form through the SHS website², hosted by the Royal Observatory, Edinburgh. Note that the SHS coverage is over a factor of two larger than the equivalent northern INT Photometric $H\alpha$ Survey (IPHAS; Drew et al. 2005) which only extends to $|b| \sim 5^\circ$. There is a small area of overlap between these two surveys. The new VST/OmegaCam Photometric $H\alpha$ Survey of the Southern Galactic Plane (VPHAS+; Drew et al., in preparation)³ is the southern counterpart of IPHAS, and also only extends to $|b| \sim 5^\circ$. VPHAS+ has been underway on the ESO VST telescope in Chile since the start of 2012, but will only supersede the utility of the SHS in the Galactic bulge and inner plane ($|b| \lesssim 5^\circ$) regions.

The SHS survey reaches a magnitude depth of approximately $R_S \simeq 20.5$ for continuum point sources, and has a faint sensitivity limit to diffuse emission of 2–5 rayleighs⁴ (see Paper I for further details). This can be compared to the approximate limit of the best Palomar Observatory Sky Survey (POSS) red plates, which used the 103a-E emulsion, of ~ 20 rayleighs (see Peimbert, Rayo & Torres-Peimbert 1975), a factor of 10 brighter than the SHS limit. Both the POSS-II (Reid et al. 1991) and UKST red plates used the IIIa-F emulsion; these plates have a sensitivity limit about twice as deep as the POSS, or $\sim 10 - 12$ R. In comparison, sky-limited narrowband CCD sensitivity limits are at the ~ 1 R level (e.g. Xilouris et al. 1996), comparable to the Southern $H\alpha$ Sky Survey Atlas (SHASSA; Gaustad et al. 2001) and the Virginia-Tech Spectral-line Survey (VTSS; Dennison, Simonetti & Topasna 1998). For summaries of past, present and upcoming $H\alpha$ surveys, see Paper I and Frew, Bojićić & Parker (2013, hereafter FBP13).

An in-depth discussion of the technical details of the SHS was presented in Paper I. The scientific exploitation of the SHS is still underway, as it has proven to be an excellent discovery medium for both extended nebulae and compact $H\alpha$ emitters. One area of particular success has been in the detection of unprecedented numbers of new Galactic planetary nebulae (PNe), published in the two Macquarie/AAO/Strasbourg $H\alpha$ (MASH) catalogues (Parker et al. 2006; Miszalski et al. 2008). While large numbers of these PNe are concentrated in the Galactic bulge (Acker, Peyaud & Parker

2006), many are found throughout the SHS footprint along the SGP. These discoveries and their subsequent spectroscopic confirmation are having a major impact on PN science (see Parker et al. 2012a, for a review).

The new MASH PNe, the recent IPHAS discoveries (e.g. Mampaso et al. 2006; Viironen et al. 2009, 2011; Sabin et al. 2010; Corradi et al. 2011), and other significant contributions (e.g. Jacoby et al. 2010; Kronberger et al. 2012) have pushed the currently known Galactic population up to more than 3200 PNe (FBP13), more than double what it was a decade ago. The SHS also proved useful for finding previously uncatalogued emission features such as knots, jets and outer halos around known PNe (e.g. Miszalski et al. 2009; Frew, Bojićić & Parker 2012; Frew et al. 2013b) and symbiotic stars (e.g. Miszalski et al. 2012).

The survey has likewise been a boon for uncovering more extended nebulae such as the optical counterparts of known Galactic supernova remnants (e.g. Stupar, Parker & Filipović 2007a; Stupar et al. 2007b; Stupar & Parker 2009, 2011, 2012; Robbins et al. 2012) seen previously only in the radio domain. Painstaking searches of the SHS by Stupar, Parker & Filipović (2008) also revealed many faint optically detected SNRs and SNR candidates not previously recognised in the radio (see also Walker, Zealey & Parker 2001; Alikakos et al. 2012). Similarly, the potential of the survey for deep optical detections of HII regions and SNRs in the LMC has been realised by Muller & Parker (2007), Bojićić et al. (2007) and Reid & Parker (in preparation).

Similarly, the SHS has also been used to study star-forming regions, both compact and diffuse (e.g. Cohen et al. 2002; Pierce 2005; Cohen et al. 2007, 2011; Zavagno et al. 2007; Urquhart et al. 2007; Cappa et al. 2008; Deharveng et al. 2009; Pinheiro et al. 2010; Russeil et al. 2005, 2010; Bik et al. 2010; Murphy et al. 2010), the diffuse interstellar medium (ISM; Tackenberg et al. 2013), Herbig-Haro objects (Girart & Viti 2007), giant Herbig-Haro outflows (e.g. Mader et al. 1999), and a range of ejecta, shell and bowshock nebulae around massive stars (e.g. Cohen, Parker & Green 2005; Gvaramadze & Bomans 2008; Gvaramadze, Kniazev & Fabrika 2010; Stock & Barlow 2010; Stock, Barlow & Wesson 2011; Duronea, Arnal & Testori 2012; Duronea, Arnal & Bronfman 2013).

Finally, the SHS has been utilised for point-source studies revealing a range of emission line-stars including WR stars (Drew et al. 2003; Morgan, Parker & Cohen 2003; Hopewell et al. 2005), Be and T Tauri stars (Pierce 2005), and cataclysmic variables (e.g. Pretorius & Knigge 2008). Importantly, using the related SHS imaging data for the LMC, Reid & Parker (2006a, b) used a deep stack of 12 $H\alpha$ and six matching SR exposures spanning the central 25 deg^2 of the LMC to uncover over 2,000 compact emission sources, including over 450 new PNe and a large number of emission-line and variable stars. These included WR stars, carbon stars, symbiotic stars, and other types of variable stars. The confirmed hot emission-line stars, 89% of which are type Be, were published together with their underlying spectral classification and luminosity type, radial and rotational velocities, $H\alpha$ fluxes, equivalent widths and photometry by Reid & Parker (2012).

1.1 Motivation for the Project

Despite these studies, the full potential of the SHS has been hampered by the lack of a clear procedure to establish a reliable, integrated $H\alpha$ flux or a surface brightness measurement for the range of distinct emission structures visible on the survey. Thus we need a reliable method to transform the pixel intensity values from Su-

¹ The effective wavelength of the short-red band is blueward of the widely used R_F system (III-aF emulsion + RG630 filter; Couch & Newell 1980), hence the name. The colour equations of this combination have been outlined by Morgan & Parker 2005.

² see <http://www-wfau.roe.ac.uk/sss/halpha/>

³ see <http://www.vphasplus.org/>

⁴ 1 rayleigh = $10^6/4\pi \text{ photons cm}^{-2} \text{ s}^{-1} \text{ sr}^{-1} = 2.41 \times 10^{-7} \text{ erg cm}^{-2} \text{ s}^{-1} \text{ sr}^{-1}$ at $H\alpha$.

perCOSMOS microdensitometer scans (e.g. Hambly et al. 1998) of the $H\alpha$ images into intensity units such as rayleighs. The procedure should also be consistent from field to field. Pierce (2005) and Paper I showed that the survey data have been well exposed to capture Galactic emission on the linear part of the photographic characteristic curve (e.g. Smith & Hoag 1979; Parker & Malin 1999). However, no detailed process for achieving reliable flux calibration for discrete sources on the SHS has yet been provided in the literature.

To address this deficiency we extend this earlier work so researchers can derive meaningful results from flux-calibrated SHS data as required, following the precepts outlined in this paper. The motivation for this study is to explore the viability of using the SHS imaging data to establish a reliable mechanism for $H\alpha$ flux measurements. This process is based on the continuum subtracted images of *non-saturated*, resolved emission sources not detected on the SHASSA (Gaustad et al. 2001), primarily due to the modest ($48''$) resolution of the latter survey. This study also attempts to address the various limitations of the base photographic data. This includes the restricted dynamic range (when scanned by the SuperCOSMOS microdensitometer) compared to the inherent photographic density range of the original films (e.g. MacGillivray & Stobie 1984; Hambly et al. 2001). In a few cases the fields are affected by high chemical fog (e.g. Tritton 1983) which further restricts the dynamic range of these survey exposures.

The structure of this paper is as follows: §2 describes the limitations of the photographic survey data and §3 describes the flux calibration process for the SHS. In §4 we focus on the derivation of SHS $H\alpha$ fluxes from the imaging data, and in §5 we undertake a comparison of the SHS fluxes for a range of discrete nebulae with independent measurements. Our conclusions and recommendations are presented in §6.

2 FLUX CALIBRATION OF THE SHS SURVEY IMAGES

The calibration of the SHS survey images is achieved by direct comparison of the continuum-subtracted SHS data with the matching continuum-subtracted SHASSA data (Gaustad et al. 2001) which provides narrowband ($H\alpha + [N II]$) and continuum images of the entire southern sky. The preliminary flux calibration process was described by Pierce (2005) and Paper I, and the reader is referred to the latter paper for technical details. Although SHASSA has a low spatial resolution with $48''$ pixels, it has the considerable advantage of being continuum subtracted and accurately flux calibrated in rayleighs, using a range of calibrating PNe from Dopita & Hua (1997). The SHASSA calibration has been verified by Finkbeiner (2003) who used the independent data from the Wisconsin H-Alpha Mapper (WHAM; Haffner et al. 2003) Northern Sky Survey at 1° resolution. Pierce et al. (2004), Pierce (2005), Frew (2008), and FBP13 also provided independent analyses of the SHASSA data. Indeed this work has recently culminated in the use of the SHASSA data to provide accurate, integrated $H\alpha$ fluxes for over 1000 Galactic PNe (FBP13).

In this paper we have completely redone the SHS calibration process afresh, by selecting data from the unvignetted ~ 25 square degree central regions (see Figure 2) of all 233 SHS fields. This was undertaken using the online⁵ $16\times$ blocked-down data for each field. These images have a resolution of $10.7''$ per pixel, and were not available in that format to Pierce (2005). These data provide a

more convenient way of working across large areas for comparison with the calibrated SHASSA data. It is important to remember that one 13° diameter SHASSA field completely covers a single 5° diameter SHS field. Of course the SHASSA survey itself suffers from artefacts resulting from the effects of bright stars (see Gaustad et al. 2001, and Figure 1).

2.1 Continuum Subtraction

Each matching SR image provide an effective measure of the continuum component for each SHS field, despite including the $H\alpha$ emission line in the bandpass. The $H\alpha$ and SR images are generally exposed to attain the same depth for continuum point sources (Paper I). However, the nature of photography and the vagaries of the observing conditions (e.g. if the exposure pairs were not contemporaneous and taken in different moon phases or if the seeing changed) mean that the SR and $H\alpha$ point source depth image quality is similar, but not exactly so. Thus, it is necessary to precisely determine a continuum-subtraction scaling factor (SF) on a field-by-field basis for the continuum subtraction process to be effective. For high-dynamic range CCD exposures, the standard method for determining the appropriate scaling factor to subtract continuum from narrow-band is to compare aperture photometry for stars on both images whose exposures are normally interleaved on short time-scales. This does not work so well with the $H\alpha$ plus SR film exposure pairs (Pierce 2005), often leading to under- or over-subtraction of the continuum. This produces positive or negative residuals around point sources, so care is needed (see §4.2).

Firstly, the $16\times$ blocked-down ($10.7''/\text{pixel}$) $H\alpha$ and SR survey images for each SHS field were obtained from the SHS website. Then, a continuum-subtracted $H\alpha(+ [N II])$ image was created from the matching $H\alpha$ and SR images in IRAF, using a scaling factor (SF), as defined in Pierce (2005) and Paper I. A range of values for the scaling factor can be applied to the SHS data until the zero-point of the continuum-subtracted SHS survey images best match the zero-point of the equivalent SHASSA data, indicating the appropriate value to use. The accuracy of the scaling factor is critical in order to avoid incorrect subtraction of the continuum component. Once a suitable SF has been determined, the continuum subtraction process works well, removing most of the stellar images and the diffuse continuum. Only stars that sit in regions with the strongest $H\alpha$ emission have been over-subtracted, and hence appear as white spots in the image, as do any high-surface brightness knots in fainter extended nebulae. For a few fields, we adopt $SF = 1$, if the comparison is inadequate to determine a formal value.

For example, Figure 1 shows four images of a $80'$ square region from field HAL0970, which shows $H\alpha$ emission at a range of intensities. The left image is the $16\times$ blocked-down SHS $H\alpha$ image, the second image is the continuum-subtracted $H\alpha$ image, the third image shows this image re-binned to a resolution to match SHASSA, while the right image shows the equivalent SHASSA data. In this example, this continuum subtraction process has worked well, removing most of the stellar images and the diffuse continuum. Only the stars that sit in the strongest emission have been over-subtracted and appear as white spots in the image. Note the residuals around stars seen in the SHASSA image, and the planetary nebula M 1-46, marked with a circle.

2.2 Calibration Factors

Each SHS field has a corresponding calibration factor (CF) determined by Pierce (2005), but these are not generally available

⁵ see http://www-wfau.roe.ac.uk/sss/halpha/hafields_online.html

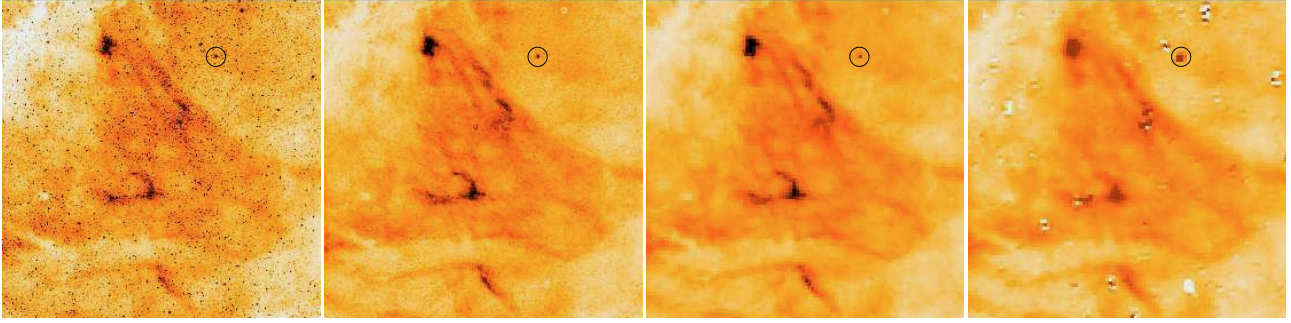


Figure 1. Comparison of SHS and SHASSA data. From left to right: (1) $H\alpha$ image of a $80' \times 80'$ region near the centre of SHS field HAL0970; (2) matching continuum-subtracted $H\alpha$ image; (3) re-binned continuum-subtracted SHS $H\alpha$ image; (4) equivalent flux-calibrated SHASSA $H\alpha$ image. Note the stellar residuals in the SHASSA image, and the planetary nebula M 1-46, highlighted with a circle in each panel. A colour version of this figure is available in the online journal.

to the community. Consequently, we have first re-calculated and improved the reliability of the CF for each survey field using our somewhat different approach based on the $16\times$ binned SHS data. In addition, in fields lacking obvious large scale emission, we have attempted to identify isolated nebulae (such as PNe) with which to provide a new calibration.

For each SHS field, we selected the corresponding SHASSA field by minimising the distance between the respective field centres. Secondly, the $16\times$ blocked-down continuum-subtracted images were re-binned and re-aligned to match the corresponding $48''$ resolution SHASSA image using the MONTAGE toolkit (<http://montage.ipac.caltech.edu/>). The SHASSA image was then cropped to the re-projected and re-binned SHS image. Now, the pixel intensity counts of the re-binned SHS images can be compared directly with the equivalent pixel intensity values (in rayleighs) from SHASSA to yield the CF for that field. The MONTAGE mProject module also returns the average value of binned pixels, which means that the final CF, derived from the pixel-to-pixel comparison with SHASSA, applies to the original full resolution SHS image. Large (typically $30' - 60'$) representative areas from the normal unvignetted area of each SHS field were selected and matched to give a robust calibration for each field. We emphasise that these regions were generally available for calibration, due to the large field-to-field overlap of the survey. This known vignetting from the $H\alpha$ filter was the original motivation for the SHS field centres being placed on a 4° grid rather than the standard 5° grid, so this problem can be avoided (see Paper I).

Figure 2 shows the blocked-down SHS $H\alpha$ image of field HAL0970 with contours of filter response at 70%, 75%, 80%, 85%, 90%, 92%, 95%, 97% and 98% of peak overlaid. Selected subregions are marked by rectangles of different colour. The magenta rectangles represent three subregions (numbered 1–3) inside the unvignetted part of the field, and the blue rectangle (region 4) includes the bright HII region M 17 (NGC 6618), also located within the unvignetted part of the field. For a comparison, the green, red and orange rectangles (regions 5–7) are areas of the field affected by filter vignetting.

A graphical plot of continuum-subtracted SHS pixel intensities against equivalent SHASSA pixel intensities should return a linear relation with a common zero point if the reduction and intensity calibration have been properly carried out and assuming the photographic intensity values are unsaturated and fall on the straight-line portion of the characteristic curve. The gradient of this plot is the CF for the image (see below). If the CF determined from

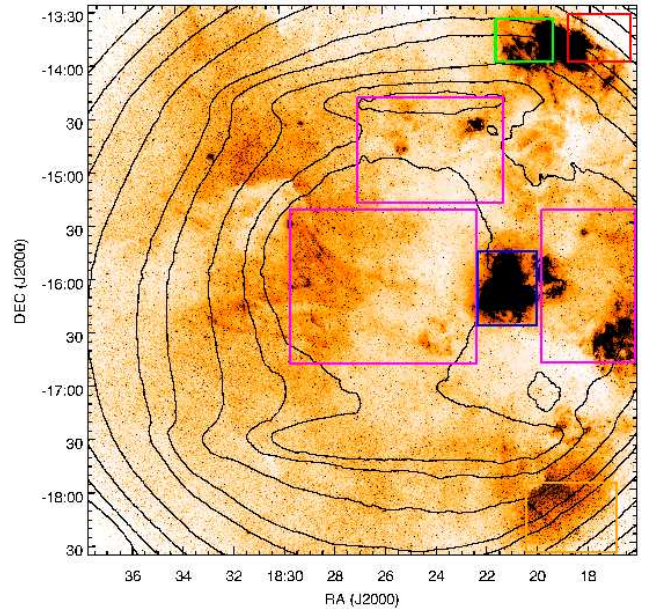


Figure 2. The full $5^\circ \times 5^\circ$ blocked-down SHS $H\alpha$ image of field HAL0970 with overlaid with contours of the filter response at 70%, 75%, 80%, 85%, 90%, 92%, 95%, 97% and 98% of peak. Selected subregions are marked by rectangles as described in the text. Those numbered 1–4 are taken from the best area of filter response and were chosen to select a range of emission line intensities. Regions 5–7 probe the edges of the field where the filter transmittance drops below 85% and are not normally accessed by the online tool. A colour version of this figure is available in the online journal.

the comparison plot is well behaved, it is applicable to full resolution SHS data for the entire field. Unfortunately, some survey fields exhibited very little diffuse emission making calibration for these fields less straightforward. In such case a careful search for small areas of discrete, low intensity $H\alpha$ emission in the unvignetted zone of the field was made, including any known large planetary nebulae. This enabled pixel by pixel comparisons between the two surveys to deliver appropriate CFs.

The process is illustrated for field HAL0970 (Figure 2). We show the calibration plot of the selected rectangular subregions as Figure 3. The points from each subregion are plotted as a different colour. The magenta points are from three subregions (1–3) inside the unvignetted part of the field, and the blue points represent the

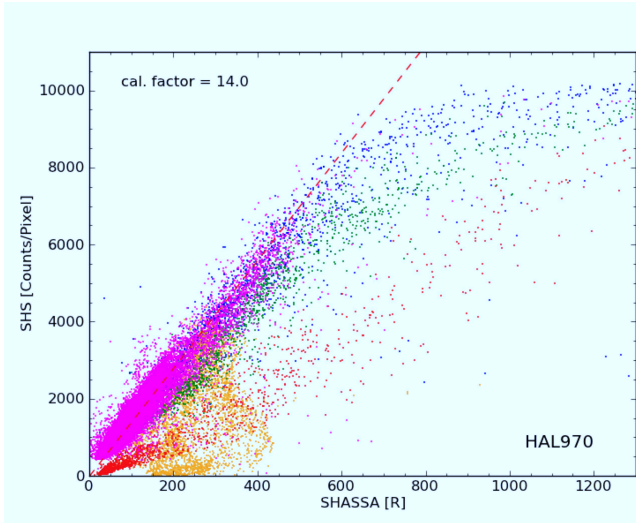


Figure 3. Calibration plot of the numbered and colour-coded subregions on field HAL0970. The magenta and blue points are from four subregions (1–4) inside the normal unvignetted part of the field, with the blue points representing the bright HII region M 17, extending to higher intensities. These align with the magenta points on the one trend, but show the effect of bright photographic saturation, seen above 500 rayleighs. The green, red and orange points show data from areas of the field (regions 5–7) affected by vignetting, and these are displaced from the magenta/blue points. A linear fit to the unvignetted data (between 50 and 500 R) is also plotted (red dashed line), with a gradient (CF) of 14.0 SHS pixel counts per rayleigh. A colour version of this figure is available in the online journal.

bright HII region M 17 (region 4), also located within the unvignetted part of the field. These align with the magenta points on the one trend, but show the effect of bright photographic saturation, seen above 500 rayleighs. A least-squares linear fit to the magenta and blue data points below 500 R is also plotted, with a gradient of 14.0 SHS pixel counts per rayleigh. This demonstrates that if provided areas are chosen from within the unvignetted field, consistent CFs are obtained giving confidence in its applicability across the field. However, if pixel-pixel comparisons are made from the subregions in Figure 3 which sample data from the vignetted regions of the field (green, red and orange points; regions 5–7), the agreement is poor and varied. The spread in SHS counts is artificial and results from applying the flat field correction to the underexposed areas of film.

We also illustrate the calibration plot for HAL0175 which is a field of intense $H\alpha$ emission centred on the Eta Carina nebula (Figure 4). Because of this, the $H\alpha$ exposure was reduced to two hours, so photographic saturation sets in at a higher than usual level of 700 – 800 R. The plot illustrates beautifully the effect of flux oversubtraction at high surface brightness, as the SR ‘continuum’ image also saturates in the brightest section of the Carina nebula. A linear fit to the data between 50 and 700 R is plotted as a red dashed line, with a gradient (CF) of 11.2 SHS pixel counts per rayleigh.

This calibration process was repeated for all 233 SHS fields. As a result, more fields now have reliable CFs than were determined by Pierce (2005) and the data are presented in Table 1. The comparison plots for six well-behaved SHS fields are shown in Figure 5. Here an essentially linear pixel-intensity relation can be seen between the SHS and SHASSA data and the linear fits are overlaid. A further six fields with some caveats are illustrated in Figure 6.

In Figure 6, we show the comparison plots for six second-

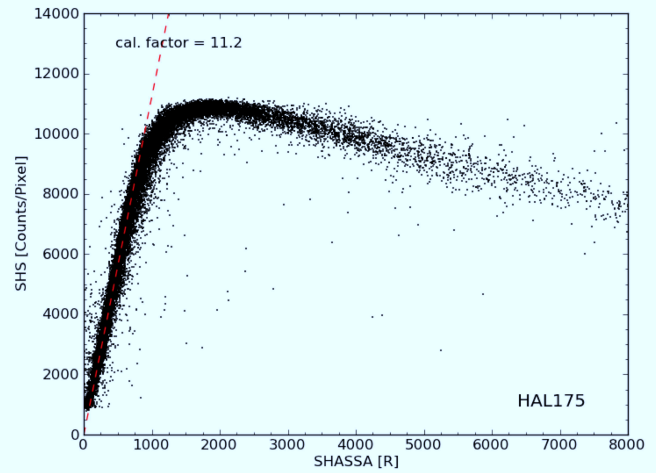


Figure 4. Calibration plot of field HAL0175 which is a field of intense $H\alpha$ emission centred on the Eta Carina Nebula. Owing to this the $H\alpha$ exposure was reduced to two hours. The plot illustrates beautifully the effect of flux oversubtraction at high surface brightness. A linear fit to the data between 50 and 700 R is also plotted, with a gradient (CF) of 11.2 SHS pixel counts per rayleigh. A colour version of this figure is available in the online journal.

ranked SHS fields, which have linear fits that are not as precise as the first-ranked fields. In the case of HAL1018, subtle changes in the $[N II]/H\alpha$ ratio across an ionization front in the large HII region IC 2177 produce a variable ratio of SHS pixel counts / R across the nebula. Furthermore, in other fields, discrete but widely separated HII regions may occur in areas of the filter response which vary at the 2–3% level. HAL0137 is such a case, where the slight inconsistencies around the linear fit seen are due to the slightly varying filter response in different areas of the field where the discrete HII regions occur. HAL1150 is an example of a field with a limited intensity range of emission, while the other fields show varying levels of photographic fog. These various effects can conspire to produce a formal fit with apparent curvature, or the appearance of two or more closely spaced trends on the calibration plot. These effects are usually small however, and should not compromise the utility of the fit in these SHS fields. The CFs determined from the linear fits can be applied with some confidence to the full (0.67'') resolution pixel data for the relevant survey field.

The SHS coverage is illustrated in Figure 7, where the quality rank for each field is colour-coded. Note that the third-ranked fields are essentially devoid of diffuse $H\alpha$ emission. Figure 8 shows the CF distribution for 170 fields (of 233) that could be fit with a linear function. The distribution of the first ranked-fields has a mean value of 11.9 ± 2.9 counts/px/R (1σ dispersion), while the second-ranked fields have a mean 12.2 ± 3.2 counts/px/R. The weighted mean is 12.0 ± 3.0 counts/px/R, which can be used as a default value for those fields without a formal CF determination. This approach then provides a direct mechanism to determine $H\alpha$ fluxes for individual emission structures not resolved by SHASSA, including, for example, many new compact MASH PNe discovered from the SHS data (e.g. Parker et al. 2006; Miszalski et al. 2008).

Table 1. Data summary for all 233 SHS survey fields. Note there are 63 fields with no formal CF determined (usually due to poor dynamic range or high chemical fog, or both). A default value of 12.0 ± 3.0 pixel counts / R can be used for these fields, as explained in the text. The table is published in its entirety as an online supplement, and a portion is shown here for guidance regarding its form and content.

Field	SF	CF (count/px/R)	Quality	Comment
HAL0067	...	(12.0)	3	small dynamic range
HAL0068	...	(12.0)	3	small dynamic range
HAL0069	...	(12.0)	3	small dynamic range
HAL0070	...	(12.0)	3	photographic fog
HAL0096	...	13.3	3	small dynamic range
HAL0097	0.98	11.4	2	
HAL0098	0.83	13.9	2	photographic fog
HAL0099	0.42	(12.0)	3	photographic fog
HAL0100	1.10	12.7	1	
HAL0101	1.12	11.7	2	small dynamic range
HAL0102	...	(12.0)	3	small dynamic range
HAL0103	0.44	6.2	2	photographic fog
HAL0131	0.62	(12.0)	3	photographic fog
HAL0132	0.91	10.0	2	
HAL0133	1.29	6.3	2	
HAL0134	1.27	10.3	1	saturates at 500 R
HAL0135	0.92	6.6	1	
HAL0136	0.87	12.0	2	
HAL0137	1.24	18.9	2	large scatter
HAL0138	0.91	8.7	2	large scatter
⋮	⋮	⋮	⋮	⋮

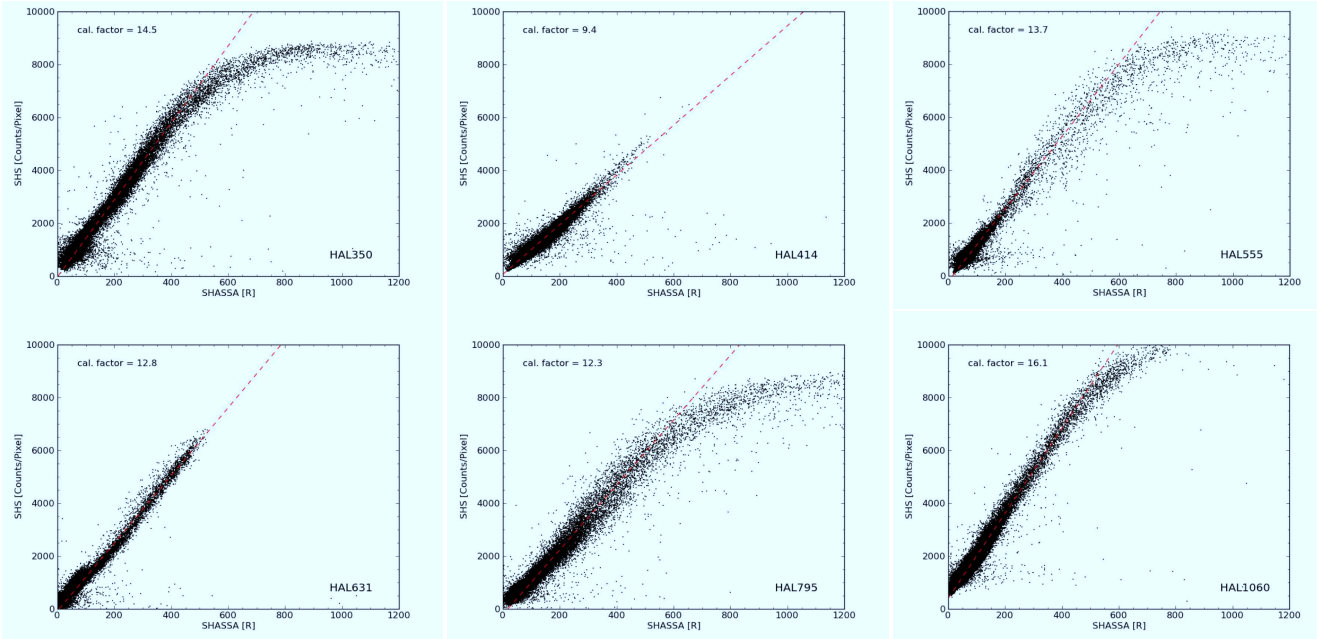


Figure 5. SHASSA-SHS pixel-by-pixel comparison plots for six first-ranked SHS fields. Some SHS fields (e.g. HAL0350, HAL0482 and HAL0555) show evidence of saturation where the intensity exceeds ~ 500 – 600 R. Below this level, most fields show a linear relation between the SHASSA and SHS. Note that fields HAL0134 and HAL1060 show evidence of photographic fog, which elevates the sky level on these SHS fields. A colour version of this figure is available in the online journal.

3 THE LIMITATIONS OF THE SHS SURVEY DATA

As previously mentioned not all SHS fields provide reliable flux measurements. Some fields are also naturally devoid of extensive $H\alpha$ emission, especially those at higher Galactic latitudes. In these cases it can be problematic to find unvignetted areas with emis-

sion features that demonstrate sufficient dynamic range to provide a large enough lever-arm for a reliable calibration.

Unlike CCD data, photographic exposures have a limited lin-

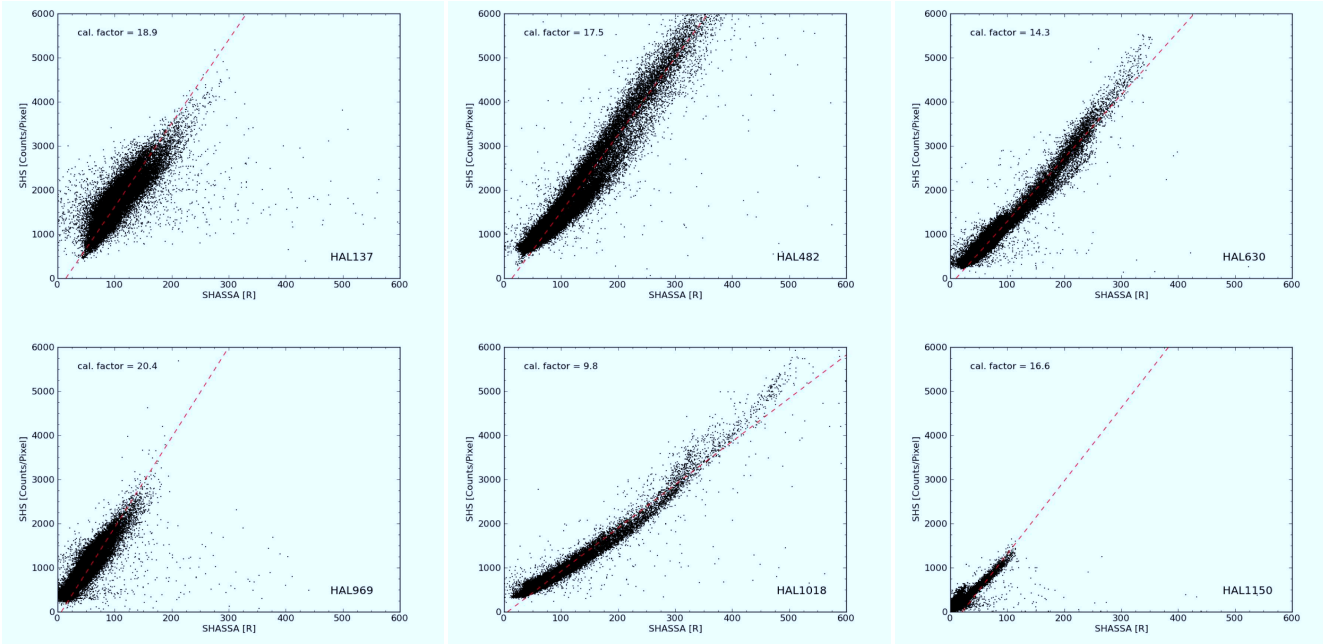


Figure 6. SHASSA-SHS pixel-by-pixel comparison plots for six second-ranked SHS fields. The slight inconsistencies around the linear fit seen in HAL137 are due to the slightly varying filter response in different areas of the field where the discrete HII regions occur. HAL1150 is an example of a field with a limited intensity range of emission, while the other five fields show varying levels of photographic fog.

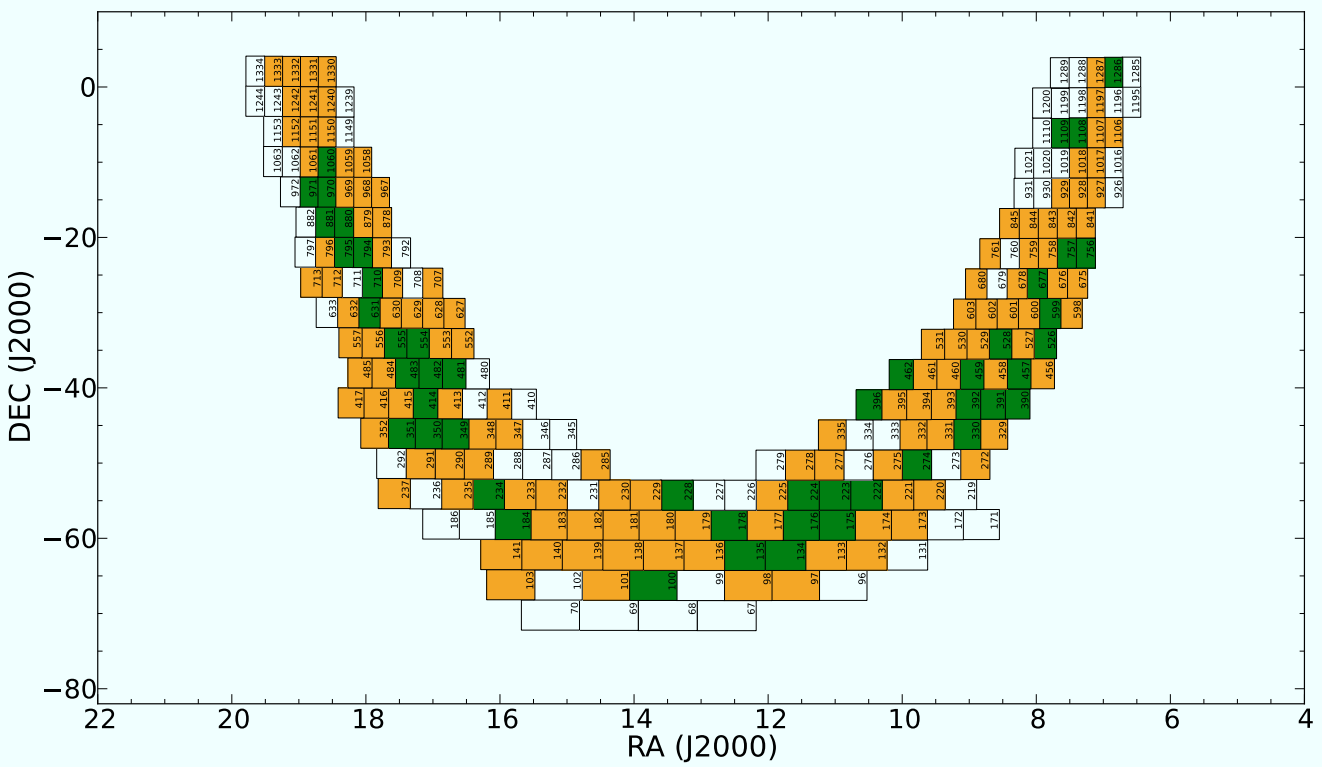


Figure 7. The sky coverage of the SHS in equatorial J2000 coordinates (note that truncated RA and DEC coordinates). The green, amber, and white boxes represent first-, second-, and third-ranked fields, respectively, and the field numbers are given. A ‘clickable’ version (though without colour-coding) is available on the SHS website. A colour version of this figure is available in the online journal.

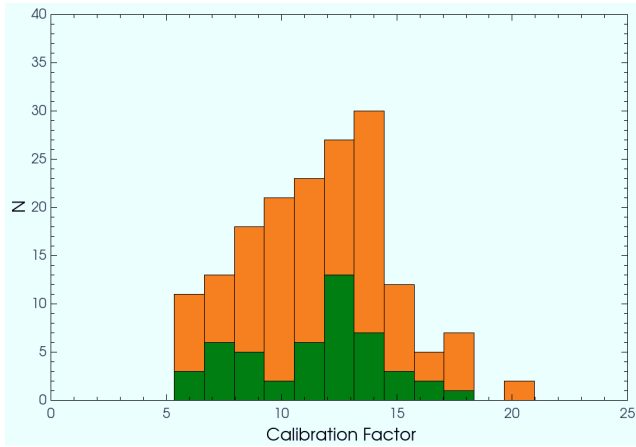


Figure 8. Histogram of derived calibration factors (CFs) for 170 SHS fields. The green and orange bars represent the numbers of first- and -second-ranked fields, respectively. A colour version of this figure is available in the online journal.

ear response and saturate at a photographic density⁶ of $D \sim 4$ (e.g. Hambly et al. 2001). However, the automated SuperCOSMOS microdensitometer used to digitise the photographic exposures imposes its own limitations, restricting the density range even further to $D \leq 2$ (Hambly et al. 1998). The data scanning and calibration processes are affected not only by the relatively low dynamic range of SuperCOSMOS, but also because some $H\alpha$ and SR pairs are not contemporaneous, being taken on different nights, and under different seeing conditions and lunar phase. Furthermore, these differences in exposure date may mean different hypersensitised emulsion batches were used which may have different levels of chemical fog and speed. Some fields have a higher than average level of photographic chemical fog due to the Tech Pan films being push-processed. These factors can introduce variations in background and sensitivity from exposure to exposure within the same ‘matching’ $H\alpha$ and SR pair.

Further uncertainties in the emission levels across survey fields can arise from the presence of continuum emission, night-sky auroral lines, and geocoronal $H\alpha$ emission as well as the effects of variable atmospheric extinction (Paper I). Ideally, all of these components would need to be disentangled to extract the true Galactic $H\alpha$ emission. In practice, the geocoronal and auroral emission is considered as a low-level, temporally varying wash, which elevates the general background on each exposure to a slightly varying degree. This is considered to be less than 2 rayleighs across the SHS (Nossal et al. (2001), based on $H\alpha$ data from the WHAM Northern Sky Survey (Haffner et al. 2003). These observations are being extended to the southern sky as the WHAM-South Survey (Haffner et al. 2010).

The original set of SHASSA and re-binned, continuum-subtracted SHS pixel-by-pixel comparison plots for selected SHS fields given by Pierce (2005) demonstrated the spread of dynamic range and linearity exhibited by the SHS data on a field by field basis. Many fields have a well defined linear trend but some are less well-behaved due to some of the factors previously mentioned. As a consequence fields were allocated a quality flag (described below) to reflect this diversity. This is based on a fresh examination of all

survey fields where each SHS field was ranked according to suitability for obtaining accurate $H\alpha$ fluxes. These ranks are given in Table 1. Representative samples of first- and second-ranked fields are shown in Figure 5 and Figure 6.

In summary, of the 233 SHS fields, 50 (21%) are well constrained by a linear fit below 500 R and so have the top ranking of 1, while a further 120 fields (52%) also have a linear fit, but with some caveats, and have been given a quality rank of 2. The 63 remaining SHS fields (27%) have little diffuse emission, making the determination of reliable CFs less straightforward, primarily due to a very restricted dynamical range of emission. A default value of 12.0 pixel counts / R can be safely used for these fields. For ease of use, we give the CF derived from the linear fit for 170 SHS fields in Table 1.

4 RELIABILITY OF THE FLUX CALIBRATION

In the previous section we have established revised calibration factors for each SHS field. In order to demonstrate the capability of these fields to provide accurate integrated fluxes for discrete sources such as PNe, HII regions, WR shells, and Herbig-Haro objects, we identified a variety of suitable calibration objects across a range of SHS fields that have independent integrated $H\alpha$ fluxes from the literature, or determined by us from SHASSA measurements. This process is described below.

4.1 Selection of Individual Sources

The object sample chosen for this flux calibration study includes a variety of astrophysical sources exhibiting a range of angular scales and emission intensities across the full range of SHS field exposure characteristics. These should be sufficient to determine if the calibration factors derived in the previous section are correct. The selected objects cover a $H\alpha$ flux range of over ~ 7 dex, and range in angular size from a few arcseconds to nearly 2° across.

The sample comprises ~ 80 PNe, several HII regions and Wolf-Rayet shells, and an isolated filament of the Vela supernova remnant. For each object the SHS $H\alpha$ flux is measured following the recipe described in §4 and is either compared with the SHASSA-derived $H\alpha$ flux from FBP13, or other independent $H\alpha$ fluxes from the literature where available. For the ejecta nebulae Hf 39 (Hen 3-519) and Wray 15-751, the $H\alpha$ fluxes, uncorrected for reddening, have been derived from the reddening-corrected fluxes and extinction values given in Stahl (1986, 1987), Hutsemekers & van Drom (1991) and Hutsemekers (1994).

4.2 Measurement Process

Suitably sized $H\alpha$ and matching SR areas of each SHS field that contain the selected calibrating objects were either downloaded as full $0.67''/\text{pixel}$ FITS images from the SHS website or extracted from the $16\times$ blocked-down data depending on the object’s angular size. The SR image was then subtracted from the $H\alpha$ equivalent in IRAF using the scaling factor provided in Table 1. This is straightforward thanks to the in-built World Coordinate System (WCS) for each field. These continuum-subtracted $H\alpha$ images were then used for flux measurements.

A photometric aperture was defined to carefully enclose the entire object in IRAF, and sky background subtraction was achieved by using a suitable sky annulus positioned to avoid stellar

⁶ The photographic density, D , is the logarithm of the ratio of incident light to transmitted light through a region of a developed emulsion.

residuals and other artefacts. Unlike SHASSA, the superior resolution of the full-resolution SHS data often enables the fine structures and extended halos of most target sources to be seen. The background-corrected photometry counts from the aperture were then used to measure the source H α flux using algorithms similar to those described in FBP13. In Figure 9 we present two examples to illustrate the fitting procedure we employ to derive sky-subtracted integrated SHS counts for our calibrating sources.

A problem can be the presence of stellar residuals within the image area of extended objects. In the Galactic plane, the stellar number density is high so residuals may also be present in the immediate region surrounding the chosen calibrator (Figure 10). Stellar residuals can sometimes appear around bright, saturated stars or compact emission sources in the continuum subtracted products (Pierce 2005; Paper I). Other challenges include residuals of the same angular size or larger than some compact PNe which partly overlap the PN image. Although these saturated residuals were removed via the same method as above, there can be some contamination of the PN emission.

Although, stellar residuals were present in the images of most objects, not all intensity contributions from these were corrected. This was because the majority of the calibrating objects studied (mainly PNe) were of moderate to large angular extent and consequently their images were populated by many small stellar residuals. Correcting for such large numbers of stellar residuals is difficult and time-consuming, and in many cases the effect of these residuals are accounted for in the sky subtraction process.

Furthermore, the SR exposures also record H α emission, which, when subtracted from the matching H α exposures, can lead to an under estimation of the true H α flux. In most cases this process appears to be self-compensating for the addition of H α emission by residuals, as our calibration results testify (see below). The integrated fluxes seem little affected for nebulae below a intensity limit of ~ 7000 counts per pixel. If the contribution to the total H α emission of a source from stellar residuals seems significant, we have attempted to apply a correction so as to provide the most accurate possible continuum subtracted H α fluxes. A correction was also applied due to the presence of a particularly bright central star, or if the calibrating object is located close to a bright, saturated star or stars being embedded in the object of interest. In the case of Hf 39, the ionizing star is prominent relative to the nebula (Figure 10). We simply measured the flux of the star with a small aperture and subtracted this from the total flux.

4.2.1 Deconvolution of [N II] Emission

Another factor that must be considered in determining H α fluxes from narrowband imaging is the close proximity of the [N II] $\lambda 6548\text{\AA}$ and $\lambda 6584\text{\AA}$ emission lines either side of H α which are included in the SHS filter bandpass (Paper I). This is the case for most Galactic sources of modest radial velocity. The contribution from the [N II] lines to the total signal through the filter can vary significantly among emission sources. For example, for Type I PNe (Peimbert 1978), the [N II]/H α ratio is usually more than three and can sometimes exceed 10 (Ruiz 1983; Corradi et al. 1997; Perinotto & Corradi 1998; Kerber et al. 1998; Tajitsu et al. 1999; Frew, Parker & Russeil 2006). This must be taken into account when comparing SHS H α fluxes with those determined independently in the literature. This can be easily done when slit spectroscopy is available as this provides the observed [N II]/H α ratio. We have chosen calibrators that have spectra available, so the [N II]/H α ratios are known. These are taken from the literature sources listed in FBP13, or else-

where. The observed ratios, usually obtained from long-slit spectroscopy, are deemed representative of the whole object which is a safe assumption in most cases, though significant internal variation across some PNe and SNRs has been observed.

The calculation of the SHS filter transmission properties is made more difficult by the blue shifting of the band pass with respect to incident angle in the fast f/2.48 converging beam of the UKST (see Parker & Bland-Hawthorn 1998). The effect was modelled by breaking down the contribution from the converging light cone into a series of concentric rings as described in Paper I. The shifting responses from each ring of the beam are weighted according to the areas of the ring and summed to generate a smeared filter response. This allows the calculation of the contributions from the [N II] lines to the total flux recorded by the survey. The reader is referred to Figure 3 of Paper I for an illustration of the modelled H α filter transmission profile. Based on the smeared-out profile, the SHS filter transmits H α at 80% and [N II] $\lambda 6548$ and $\lambda 6584\text{\AA}$ at 82% and 50% respectively. Given that the intrinsic ratio between the $\lambda 6548\text{\AA}$ and $\lambda 6584\text{\AA}$ [N II] line strengths is quantum mechanically fixed at ~ 3.0 , the SHS filter transmits approximately 58% of [N II], compared to 80% transmission of the H α flux. This gives a [N II]/H α filter transmittance ratio of 0.725 which is the constant in equation 2, below.

While the filter transmission falls towards the off-axis edge of each survey field (see Figure 2), this is not considered significant in this study due to the purposely large overlap between adjacent SHS fields on a 4-degree grid (Paper I). This enables the data of interest to be preferentially selected from the non-vignetted central region of an available field. The filter transmission constant will vary at large off-axis angular distances but this is only relevant for the few fields at the eastern edges of the SHS region.

4.3 SHS H α Fluxes

The equation used to derive the integrated SHS H α + [N II] (or ‘red’) flux is essentially the same as the expression given in FBP13. The SHS red flux in cgs units is given by:

$$F_{\text{red}} = 5.66 \times 10^{-18} \times P_S^2 \times \left(\frac{\text{SUM}}{\text{CF}} \right) \text{ erg cm}^{-2} \text{ s}^{-1} \quad (1)$$

where the first constant in the expression is the conversion factor from rayleighs to cgs units, P_S is the ‘plate scale’ of the digital SHS data (0.67'' per pixel for the full resolution images, and 10.7'' for the 16 \times blocked-down images). The summed counts obtained from the aperture photometry procedure (SUM) need to be divided by the relevant calibration factor, CF , taken from table 1, in order to determine the integrated red flux in units of $\text{erg cm}^{-2} \text{ s}^{-1}$. The SHS field number can be obtained from the header of any downloaded FITS image.

The integrated H α flux is then obtained by correcting for the contribution from the contaminant [N II] lines (Frew 2008; FBP13) and is given by the following expression:

$$F(\text{H}\alpha)_{\text{SHS}} = \frac{F_{\text{red}}}{K_{\text{tr}} R_{[\text{N II}]} + 1} \quad (2)$$

where $R_{[\text{N II}]}$ is the observed spectroscopically determined [N II]/H α ratio for the emission object in question (mainly PNe) and the constant, $K_{\text{tr}} = 0.725$, takes into account the throughput of the SHS filter. Following FBP13, the [N II] flux refers to the sum of the $\lambda 6548$ and $\lambda 6584$ lines. If only the brighter $\lambda 6584$ line is mea-

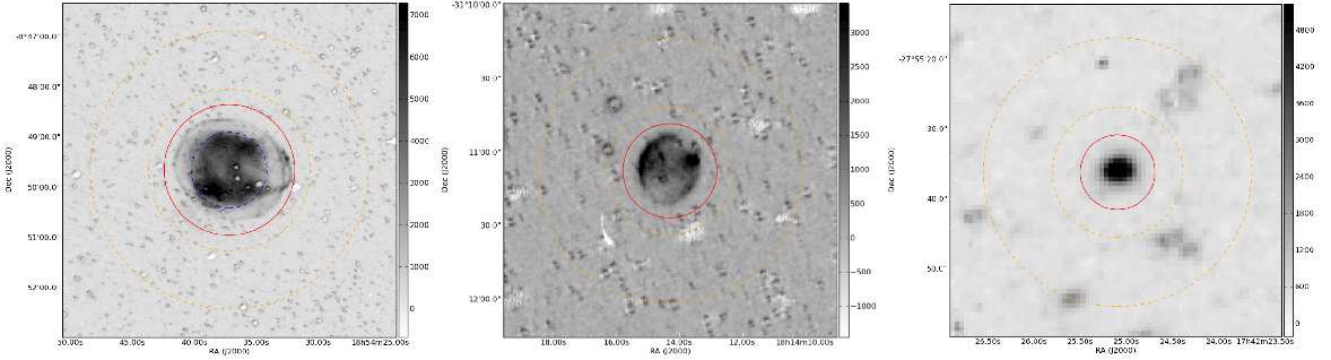


Figure 9. SHS continuum-subtracted images showing the photometric apertures (red circles) and background sky annuli (yellow circles) for three PNe: IC 1295 (left), SB 4 (middle) and the compact object JaSt 36 (right). The images are $400''$, $135''$, and $50''$ on a side, respectively, and have NE at top left. A colour version of this figure is available in the online journal.

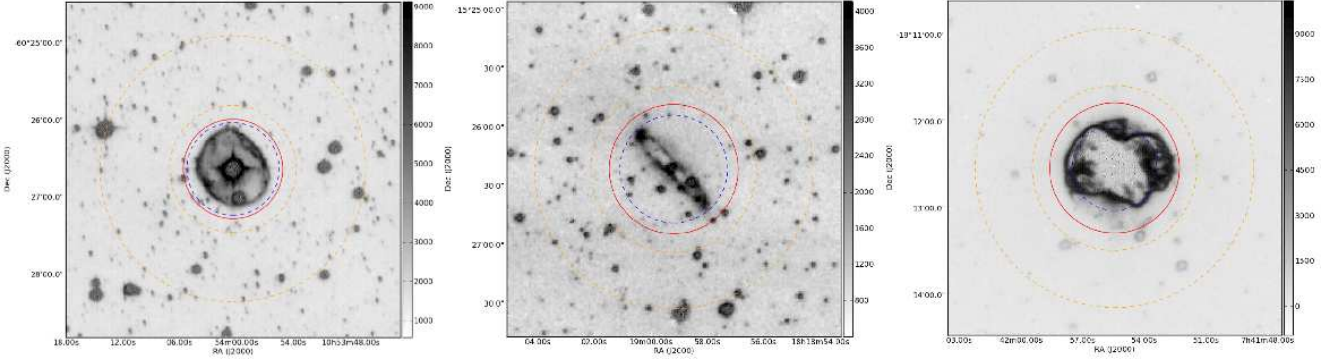


Figure 10. SHS continuum-subtracted images illustrating the effect of a bright stellar residual from the massive WN11 star, Hen 3-519 (in its surrounding nebula, Hf 39, left), several residuals, including from the binary central star of the toroidal PN, PHR J1818-1526 (middle), and a very bright, saturated PN with flux over-subtraction in its interior (NGC 2440, right). The catalogued diameter is given by the blue dashed circle in each figure, and the photometric apertures and background sky annuli are selected as before. The images are $170''$, $320''$, and $230''$ on a side, respectively, and have NE at top left. A colour version of this figure is available in the online journal.

surable in a spectrum, $F[\text{N II}]$ is estimated as $1.33 \times F(\lambda 6584)$ as the 6584 to $6548\text{\AA}[\text{N II}]$ line ratio is 3:1.

The uncertainty budget for the SHS $\text{H}\alpha$ flux is determined following the procedure presented in FBP13. Additionally, the uncertainty in the CF for the particular SHS field, as measured from the fit, was added in quadrature to the uncertainty in aperture intensity counts.

We emphasise that the $[\text{N II}]$ transmission differs between the SHS and the SHASSA survey filters (70\AA and 32\AA FWHM respectively), so the SHS filter passes considerably more $[\text{N II}]$ emission. The transmissible $[\text{N II}]/\text{H}\alpha$ ratios of the two survey filters are 0.725 and 0.375 respectively. In the original calibration of the SHS from SHASSA data (Paper I), both HII regions and the diffuse ionized gas were assumed to have negligible $[\text{N II}]$ emission. However, the median $[\text{N II}]/\text{H}\alpha$ ratio for a large number of Galactic HII regions is actually ~ 0.4 (derived from the data graphically presented by Frew & Parker 2010), which is in reasonable agreement with the average $\lambda 6584/\text{H}\alpha$ ratio of ~ 0.3 seen in a sample of faint HII regions (Madsen et al. 2006a). These authors also noted that the $\lambda 6584/\text{H}\alpha$ ratio in the warm interstellar medium (WIM) generally increased below an $\text{H}\alpha$ intensity of 10 rayleighs, approaching unity at the faintest measured intensities. Owing to these points, there is an offset of ~ 10 – 15 per cent in the flux obtained from using the CF

values presented in Table 1. We therefore recommend that the formally determined SHS $\text{H}\alpha$ fluxes given by equation 2 be increased by this factor; i.e. the logarithmic $\text{H}\alpha$ fluxes should be brightened by 0.05 dex.

The total uncertainty on the SHS $\text{H}\alpha$ flux is given by the following expression, which includes a SHASSA uncertainty term as the SHS is bootstrapped to this survey:

$$\sigma_{F(\text{H}\alpha)}^2 = \sigma_{\text{phot}}^2 + \sigma_R^2 + \sigma_{\text{cal}}^2 + \sigma_{\text{SHASSA}}^2 \quad (3)$$

where σ_{phot} is the proportional uncertainty in the photometry measurement, σ_R is the uncertainty in the deconvolved $\text{H}\alpha$ flux due to the uncertainty in $R_{[\text{N II}]}$, σ_{cal} is the calibration uncertainty for the respective SHS field, and σ_{SHASSA} is the known SHASSA calibration uncertainty of 8% (Gaustad et al. 2001).

4.3.1 Emission Measures

The SHS pixel data can also be used in the study of the warm interstellar medium (WIM) and low-surface brightness HII regions on spatial scales down to 3 – $5''$, showing fine detail that is not seen on SHASSA. For ionized hydrogen, the surface brightness, $S_{\text{H}\alpha}$ (in rayleighs) and the emission measure (EM, in units of cm^{-6}pc) are

related by the following expression (Haffner et al. 2003; Madsen, Reynolds & Haffner 2006a; cf. Reynolds & Ogden 1982):

$$EM = \int n_e dl = 2.75 t^{0.9} S_{H\alpha} e^{2.2E(B-V)} \text{ cm}^{-6} \text{ pc} \quad (4)$$

where t is the electron temperature in units of 10^4 K. As before, the pixel counts can be converted into rayleighs using the CF for the specific SHS field, and then the contribution from the contaminant [N II] lines need to be deconvolved from the total measured intensity to determine an $H\alpha$ surface brightness or emission measure (see §4.2.1). The resulting data has wide application to the study of the structure and ionization of HII regions and the WIM.

5 COMPARISON OF SHS $H\alpha$ FLUXES AGAINST INDEPENDENT ESTIMATES

Table 2 gives our measured SHS $H\alpha$ fluxes for selected PNe and other calibrating emission-line sources. The fluxes are based on our newly determined individual field calibrations. We also list the independent integrated $H\alpha$ fluxes for these objects. The SHASSA $H\alpha$ fluxes are primarily taken from FBP13, or measured here in the same manner, while $H\alpha$ fluxes for the other nebulae are drawn from Stahl (1987), Hutsemekers (1994), Nota et al. (1995), Duerbeck & Benetti (1996), Weinberger, Kerber & Gröbner (1997), Polacco (1999), Beaulieu, Dopita & Freeman (1999), Boumis et al. (2003, 2006), Jacoby & Van de Steene (2004), Ruffe et al. (2004), Madsen et al. (2006b), Parker et al. (2011, 2012b), and Frew et al. (2013b). FBP13 showed that the flux uncertainties from Cappelaro et al. (2001) are substantial, so we have not used these in our comparison.

Figure 11 presents our SHS $H\alpha$ fluxes plotted against independent measurements from the literature for all 101 objects in the calibrating sample. A tight linear relation is obtained over a range of 7 dex (10 million) in integrated $H\alpha$ flux. The lower panel plots the offset (in the sense of SHS minus literature) against the SHS flux. Unsurprisingly the first-ranked fields permit the measurement of the most accurate fluxes, and the measurement accuracy is slightly less for second ranked fields. Our fluxes show a dispersion with the literature data of 0.12 dex from first-ranked fields, and 0.15 dex for second-ranked fields. Considering the uncertainties on the literature fluxes, this translates to a nominal uncertainty of 0.10 dex and 0.14 dex, respectively. This shows that photographic data, if carefully considered is a useful source for emission-line intensities and fluxes (see also the flux data from Abell (1966), as reduced by FBP13).

In Figure 12, we show the offset between the SHS and literature $H\alpha$ flux plotted as a function of $H\alpha$ surface brightness (in $\text{erg cm}^{-2} \text{ s}^{-1} \text{ sr}^{-1}$), in turn derived from the literature flux and the angular size of the object. The sample is comprised of all the objects from Table 2, plus another 45 saturated PNe, including very bright PNe like NGC 3918 and NGC 2440 (Figure 10). The fluxes for the bright PNe are taken from FBP13 (and references therein) and the angular diameters are from Tylenda et al. (2003), Frew (2008), or the references given in the footnotes to Table 2. The twin effects of photographic saturation and flux over-subtraction occur for the brighter nebulae with a surface brightness, $\log S(H\alpha) \geq -4.0 \text{ erg cm}^{-2} \text{ s}^{-1} \text{ sr}^{-1}$, where an inflection point in the plot is clearly seen.

In a follow-up paper (Bojičić et al., in preparation), we will provide new $H\alpha$ fluxes for all measurable PNe found in the SHS

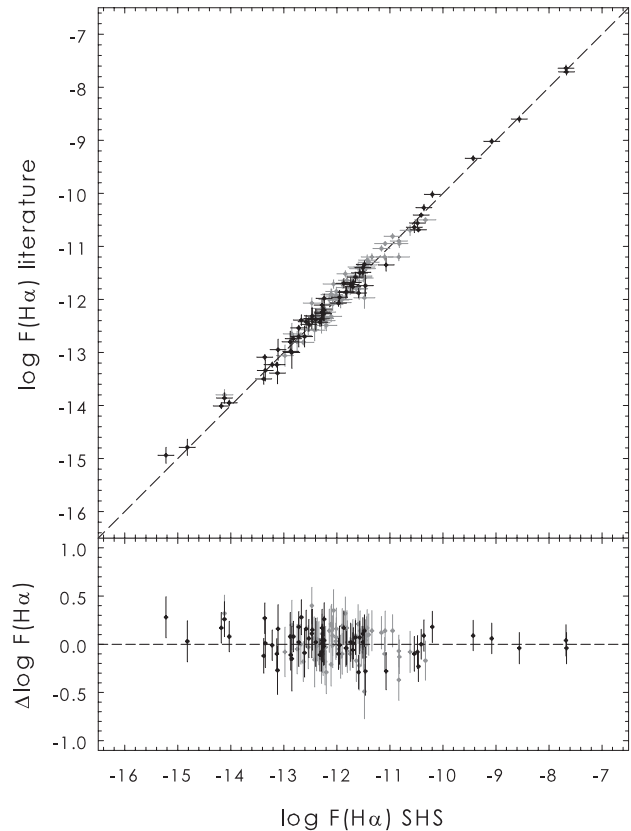


Figure 11. SHS versus literature $H\alpha$ fluxes for the whole sample of unsaturated calibrating sources. Fluxes derived from first- and second-ranked fields are plotted with filled and open circles, respectively. The agreement is excellent over a range in flux of more than 10 million. The lower panel plots the delta flux, in the sense of SHS minus literature fluxes.

footprint, that cannot be measured from SHASSA due to their faintness and/or compact size. These fluxes will complement the recent flux catalogue of FBP13. In particular, the new SHS $H\alpha$ fluxes for faint Galactic bulge PNe will be valuable, as they can be compared with new radio continuum fluxes (e.g. Bojičić et al. 2011a,b) to estimate extinction values, or compared with integrated fluxes in other wavebands; e.g. the [O III] fluxes of Kovacevic et al. (2011), in order to investigate the faint end of the bulge PN luminosity function in different emission lines (e.g. Ciardullo 2010).

6 POINT SOURCE PHOTOMETRY

For completeness, we give a brief account of the SHS as a provider of photometric data for point-source emitters. Each $H\alpha$ and matching SR survey field has been automatically processed through the standard SuperCOSMOS photometric and image processing pipelines (e.g. Hambly et al. 1998, 2001). These provide so-called IAM (image-analysis mode) data for detected point-source and compact extended sources in each survey passband above a locally thresholded background. An image-deblending algorithm based on areal profile fitting at image levels equally spaced in log (intensity) is also applied (e.g. Beard, McGillivray & Thanisch 1990; Hambly, Irwin & MacGillivray 2001) which can be useful in crowded fields such as the Galactic plane. Consequently, large catalogues of detected sources, including accurate positions, photometry and

Table 2. A comparison of our SHS H α fluxes for 88 PNe and 13 other nebulae with independent integrated H α fluxes taken from the literature, as explained in the text. The table is published in its entirety as an online supplement, and a portion is shown here for guidance regarding its form and content.

Name	$\log F(\text{H}\alpha)$ (other)	Reference	$\log F(\text{H}\alpha)$ (SHS)	SHS Field	Remarks
Abell 18	-12.00 ± 0.09	FBP13	-11.92 ± 0.09	HAL1197	...
Abell 23	-11.86 ± 0.09	FBP13	-11.82 ± 0.08	HAL0526	...
Abell 26	-12.24 ± 0.08	FBP13	-12.31 ± 0.15	HAL0601	...
Abell 27	-12.01 ± 0.05	FBP13	-12.01 ± 0.15	HAL0602	...
Abell 44	-11.49 ± 0.10	FBP13	-11.56 ± 0.08	HAL0970	...
Abell 45	-11.26 ± 0.10	FBP13	-11.35 ± 0.15	HAL1060	...
Abell 48	-11.58 ± 0.06	FBP13b	-11.55 ± 0.10	HAL1241	...
Abell 58	-12.28 ± 0.06	FBP13	-12.32 ± 0.11	HAL1333	...
BMP J1613-5406	-11.60 ± 0.09	FBP13	-11.50 ± 0.12	HAL0289	...
BMP J1808-1406	-11.68 ± 0.09	FBP13	-11.78 ± 0.14	HAL0969	...
CGMW 3-2111	-12.38 ± 0.10	B06, FBP13	-12.40 ± 0.10	HAL1058	...
CVMP 1	-11.50 ± 0.10	FBP13a	-11.63 ± 0.14	HAL0232	...
DPV 1	-12.5 ± 0.3	DB96, P99	-12.50 ± 0.11	HAL0968	Sakurai's object
FP J0711-2531	-10.69 ± 0.04	FBP12	-10.51 ± 0.11	HAL0756	...
FP J1824-0319	-10.40 ± 0.10	M06, FBP13	-10.44 ± 0.10	HAL1240	...
Fr 2-7	-10.82 ± 0.10	FBP13	-10.86 ± 0.12	HAL0097	...
G4.4+6.4	-11.25 ± 0.06	FBP13	-11.31 ± 0.10	HAL0878	...
GL1PN J1530-5557	-13.86 ± 0.10	PC12 ^a	-14.17 ± 0.12	HAL0233	...
GL1PN J1557-5430	-14.79 ± 0.15	PC12 ^a	-14.70 ± 0.15	HAL0234	...
GL1PN J1642-4453	-14.94 ± 0.15	PC12 ^a	-14.88 ± 0.15	HAL0413	...
⋮	⋮	⋮	⋮	⋮	⋮

Reference codes: ASTR91 – Acker et al. (1991); B03, B06 – Boumis et al. (2003, 2006); BDF99 – Beaulieu et al. (1999); DB96 – Duerbeck & Benetti (1996); F13 – this work; FBP13 – Frew et al. (2013a); FBP13b – Frew et al. (2013b); H94 – Hutsemekers (1994); HDM98 – Hua, Dopita & Martinis (1998); JaSt04 – Jacoby & Van de Steene (2004); KH93 – Kistiakowsky & Helfand (1993); FPR06 – Frew et al. (2006); M06 – Madsen et al. (2006); P99 – Pollacco (1999); PC12 – Parker et al. (2012); PFM11 – Parker et al. (2011); RZ04 – Ruffle et al. (2004); S87 – Stahl (1987); SK89 – Shaw & Kaler (1989); WKG97 – Weinberger et al. (1997); XP94 – Xilouris et al. (1994); XPPT – Xilouris et al. (1996).

Notes: ^a Fluxes revised using updated calibration factors.

other image parameters are provided for each field from the SHS website⁷. A significant advantage of the SHS data is the ability to detect point sources that have been photometrically calibrated to CCD standards (e.g. Boyle, Shanks & Croom 1995; Croom et al. 1999). The narrowband H α images are also calibrated to an ‘*R*-equivalent’ scale.

The 3-hour H α and 15-min broad-band SR exposure times are chosen so that both reach similar depths of $R_S \simeq 20.5$ for point sources (Paper I). Where an object is detected in one band but not in the other, a default value of 99.999 is given in the online IAM catalogue data for the magnitude in the missing bandpass. Positional and magnitude-dependent errors are corrected for in the data that are available through the SHS website. Photometric consistency is achieved by using the field overlap regions to establish zero-points across the survey. These corrected magnitudes provide a means, for example, of selecting point-source H α emitters by looking for significant brightening on the H α source compare to its SR counterpart, especially when combined with the SSS *I*-band photometry which effectively eliminates late-type stellar contaminants (Paper I). The IAM data was successfully used by Pierce (2005) to discover a range of emission-line stars, by Hopewell et al. (2005) who found several WO and WC stars, and in the discovery of numerous compact PNe by Miszalski et al. (2008).

Modest variations in measured IAM stellar parameters from SHS data occur as a function of field position and the resulting variable PSF due to the effects of field rotation on the sky. This is

apparent when comparing point sources taken on the long 3 hour H α exposures with the short 15 min SR exposures, and also from field vignetting, especially at large radii from the field centres. To better account for such effects requires that photometric comparisons are performed over limited 1-degree areas such that the true H α emitters show a bona-fide enhanced H α magnitude compared with the continuum *SR* magnitude. At the bright end of the magnitude distribution, severe saturation effects also come in to play, limiting stellar photometry to *R* of about ~ 12 in both the H α and *SR* passbands. Further details are given in Paper I.

7 CONCLUSIONS AND RECOMMENDATIONS

We have established calibration factors (Table 1) for 170 of the 233 SHS fields (73 per cent), so these can be used directly to derive accurate integrated H α fluxes for a wide range of objects including PNe, HII regions, Wolf-Rayet shells and supernova remnants (refer to Figure 11). Based on the significant number of calibrating objects we have used, we can demonstrate that our derived fluxes agree to within ± 0.1 dex with independent fluxes from the literature over a remarkable range of 7 dex in integrated flux. There is a small systematic offset where SHS fluxes seem to be approximately 10–15% fainter than the equivalent SHASSA fluxes. The origin of this offset is attributed to the differing filter transmission of the [N II] lines between SHASSA and the SHS, and the fact that the original analysis assumed that the diffuse emission from the ISM was solely H α emission. Better agreement can be obtained by scaling up the SHS H α fluxes by 0.05 dex.

⁷ <http://www-wfau.roe.ac.uk/sss/halpha/>

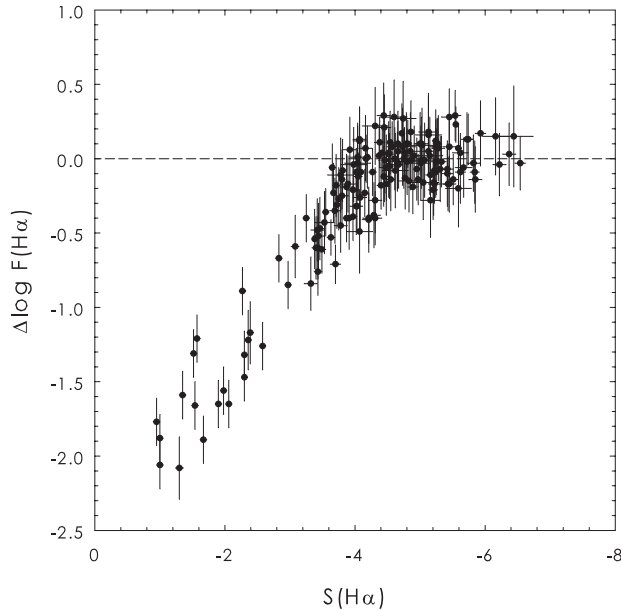


Figure 12. The offset between SHS and literature $H\alpha$ fluxes plotted as a function of $H\alpha$ surface brightness (in $\text{erg cm}^{-2} \text{s}^{-1} \text{sr}^{-1}$) derived from the literature flux. The twin effects of photographic saturation and flux over-subtraction occur for the brighter nebulae with a surface brightness, $\log S(H\alpha) \geq -4.0 \text{ erg cm}^{-2} \text{s}^{-1}$.

Determining fluxes for extended objects within the first-ranked SHS fields can be performed with confidence. This is to be expected since these fields exhibit a tight linear data-data relation with respective SHASSA images. For most of the second-ranked fields, the flux uncertainties are somewhat larger, though still usable. There are currently 63 relatively featureless fields in Table 1) for which we could not determine the CF. These fields either have high chemical fog levels or the fields have a poor dynamic range. This does not mean there is anything wrong per se with the exposures, just that the fields are mostly devoid of variable intensity $H\alpha$ emission making it difficult to determine the CF. Such fields may still contain significant numbers of small localised emission nebulae such as PNe. In the meantime, we use the mean CF for all first-ranked fields of $12.0 \text{ counts px}^{-1} \text{R}^{-1}$ as a default value for fields with indeterminate values. The $H\alpha$ surface brightnesses and integrated fluxes so derived should be accurate to better than ± 0.2 dex. Many of these fields still could be used with more confidence if local CF values were established, even for fields affected by high chemical fog.

The adopted value for the SF and CF and rank status of each of the 233 SHS fields are given in Table 1 and is the main legacy material from this work. The fields can be used not just for exploratory science and discovering new astronomical objects, but now for also deriving their integrated $H\alpha$ fluxes and surface brightnesses. The SHS will remain useful for many years to come, and will be superseded by the new VPHAS+ $H\alpha$ survey (J. Drew et al., in preparation) only in the region along the SGP within $|b| \leq 5^\circ$. Even there, the SHS will be the source of first-epoch properties for emission-line stars and other exotica for future studies on variability.

In summary, the following notes and caveats should be considered when using the SHS data to provide $H\alpha$ intensities and integrated flux measurements:

1. The pixel data has been treated by a filter flat-field as described

in Paper I. This is a one-off correction that is assumed valid for all survey fields.

2. We recommend that objects located more than 1.8° from the SHS field centre not be measured for flux if accuracy is a requirement. Excepting for the fields on the east, south and northern edges of the SHS zone, the generous overlap between field centres means that a neighbouring field should be available for flux measurement. Note that when full $0.67''/\text{pixel}$ resolution areas are obtained from the SHS webpage using the “Get Image” tool, the best data is automatically selected from the unvignetted central region of an available field.
3. The effect of geocoronal $H\alpha$ emission should be low. Paper I found from a random sample of six SHS fields that the Earth shadow height for the whole 3-hour observation and across the five-degree field of view was greater than 6000 km, so low-level geocoronal emission ($< 2 \text{ R}$) is not problematic, as most SGP fields covered by the SHS will contain significantly stronger diffuse emission.
4. Telluric OH emission may contaminate the images at low flux levels, but this is also altitude dependent and can be safely ignored.
5. The image data is non-linear at high intensities. Photographic saturation sets in at around 500 – 600 R, or approximately 6000 – 7000 counts per pixel (for a typical CF value). Objects showing values above this, or showing ‘negative’ residuals after continuum subtraction should be treated with caution, and the total fluxes can be considered to be firm lower limits. Consider point-source algorithms if the nebula is bright and compact.
6. Brighter nebulae that are too extended for the application of point-source algorithms should be conspicuous enough to be detected in SHASSA. We recommend the use of this survey in such cases.
7. Integrated fluxes accurate to $\pm 0.1 - 0.15$ dex, can be generally obtained across the survey fields, with the second-ranked fields have slightly larger systematic errors.
8. Pending a more detailed analysis, a CF of $12.0 \pm 3.0 \text{ counts px}^{-1} \text{R}^{-1}$ can be used as a default value for the 63 fields with no formal determination (see Figure 7). The integrated $H\alpha$ fluxes for any objects derived from these fields should be accurate to better than ± 0.2 dex. Alternatively, any known PNe or other small nebulae with an independent flux can be used to calibrate the whole field, but only if they are below the saturation limit. In such cases, the CF value for the field can be treated as a free parameter and varied until the measured integrated SHS flux matches the independent value.
9. Emission from the red [N II] lines often contributes significantly to the $H\alpha + [\text{N II}]$ flux, especially for PNe and SNRs. This contribution needs to be carefully de-convolved from the total flux using the observed spectroscopic ratio for individual objects, and following the procedure described in §4.3.
10. Owing to the different passbands of the SHASSA and SHS filters, the SHS $H\alpha$ fluxes determined from Equation 2 should be increased by an additional factor; i.e. the logarithmic $H\alpha$ fluxes should be brightened by 0.05 dex.
11. The nature of photography and the scanning process produces a range of artefacts and spurious images on the SHS. The user should be aware of these, and can find more details in Paper I.

ACKNOWLEDGMENTS

This research used data from the AAO/UKST H α Survey, produced with the support of the Anglo-Australian Telescope Board and the UK Particle Physics and Astronomy Research Council (now the STFC), and data from the Southern H α Sky Survey Atlas (SHASSA), which was produced with support from the National Science Foundation. This research made use of the SIMBAD database, operated at the CDS, Strasbourg, and also made use of Montage, funded by the National Aeronautics and Space Administration's Earth Science Technology Office, Computation Technologies Project, under Cooperative Agreement Number NCC5-626 between NASA and the California Institute of Technology. Montage is maintained by the NASA/IPAC Infrared Science Archive. DJF is grateful to Macquarie University for the award of a research fellowship, and ISB thanks the ARC for his Super Science Fellowship (project ID FS100100019). QAP acknowledges support from Macquarie University and the Australian Astronomical Observatory and MG thanks the Australian Government for an Australian Postgraduate Award.

REFERENCES

- Abell G.O., 1966, *ApJ*, 144, 259
- Acker A., Peyaud A.E.J., Parker Q., 2006, *Proc. IAU Symp.*, 234, 355
- Acker A., Stenholm B., Tylen R., Raytchev, B., 1991, *A&AS*, 90, 89
- Alikakos J., Boumis P., Christopoulou P.E., Goudis C.D., 2012, *A&A*, 544, A140
- Beard S.M., MacGillivray H.T., Thanisch P.F., 1990, 247, 311
- Beaulieu S.F., Dopita M.A., Freeman K.C., 1999, *ApJ*, 515, 610
- Bik A. et al., 2010, *ApJ*, 713, 883
- Bojičić I.S., Filipović M.D., Parker Q.A., Payne J.L., Jones P.A., Reid W., Kawamura A., Fukui Y., 2007, *MNRAS*, 378, 1237
- Bojičić I.S., Parker Q.A., Filipović M.D., Frew D.J., 2011a, *MNRAS*, 412, 223
- Bojičić I.S., Parker Q.A., Frew D.J., Vaughan A.E., Filipović M.D., Gunawardhana M.L.P., 2011b, *AN*, 332, 697
- Boumis P., Paleologou E.V., Mavromatakis F., Papamastorakis J., 2003, *MNRAS*, 339, 735
- Boumis P., Akas S., Xilouris E.M., Mavromatakis F., Kapakos E., Papamastorakis J., Goudis C.D., 2006, *MNRAS*, 367, 1551
- Boyle B.J., Shanks T., Croom S.M., 1995, *MNRAS*, 276, 33
- Cappa C., Niemela V.S., Amorín R., Vasquez J., 2008, *A&A*, 477, 173
- Cappellaro E., Sabbadin F., Benetti S., Turatto M., 2001, *A&A*, 377, 1035
- Ciardullo R., 2010, *PASA*, 27, 149
- Cohen M., Green A.J., Parker Q.A., Mader S., Cannon R.D., 2002, *MNRAS*, 336, 736
- Cohen M., Parker Q.A., Green A.J., 2005, *MNRAS*, 360, 1439
- Cohen M. et al., 2007, *ApJ*, 669, 343
- Cohen M., Parker Q.A., Green A.J., Miszalski B., Frew D.J., Murphy T., 2011, *MNRAS*, 413, 514
- Condon J.J., Kaplan D.L., 1998, *ApJS*, 117, 361
- Condon J.J., Kaplan D.L., Terzian Y., 1999, *ApJS*, 123, 219
- Corradi R.L.M., Villaver E., Mampaso A., Perinotto M., 1997, *A&A*, 324, 276
- Corradi R.L.M. et al., 2011, *MNRAS*, 410, 1349
- Couch W.J., Newell E.B., 1980, *PASP*, 92, 746
- Croom S.M., Ratcliffe A., Parker Q.A., Shanks T., Boyle B.J., Smith R.J., 1999, *MNRAS*, 306, 592
- Davies R.D., Elliott K.H., Meaburn J., 1976, *MNRAS*, 81, 89
- Davies R.D., Elliott K.H., Goudis C., Meaburn J., Tebbutt N.J., 1978, *A&AS*, 31, 271
- Deharveng L., Zavagno A., Schuller F., Caplan J., Pomarès M., De Breuck C., 2009, *A&A*, 496, 177
- Dennison B., Simonetti J.H., Topasna G.A., 1998, *PASA*, 15, 147
- DePew K., Parker Q.A., Miszalski B., De Marco O., Frew D.J., Acker A., Kovacevic A.V., Sharp R.G., 2011, *MNRAS*, 414, 2812
- Dopita M.A., Hua C.T., 1997, *ApJS*, 108, 515
- Drew J.E., Barlow M.J., Unruh, Y.C., Parker Q.A., Wesson R., Pierce M.J., Masheder M.R.W., Philipps S., 2004, *MNRAS*, 351, 206
- Drew J.E. et al., 2005, *MNRAS*, 362, 753
- Duerbeck H.W., Benetti S., 1996, *ApJ*, 468, L111
- Duronea N.U., Arnal E.M., Testori J.C., 2012, *A&A*, 540, A121
- Duronea N.U., Arnal E.M., Bronfman L., 2013, *A&A*, 551, A71
- Elliott K.H., Meaburn J., 1976, *Ap&SS*, 39, 437
- Elliott K.H., Goudis C., Meaburn J., 1976, *MNRAS*, 175, 605
- Finkbeiner D.P., 2003, *ApJS*, 146, 407
- Frew D.J., 2008, PhD thesis, Macquarie University
- Frew D.J., Parker Q.A., 2006, *Proc. IAU Symp.*, 234, 49
- Frew D.J., Parker Q.A., 2010, *PASA*, 27, 129
- Frew D.J., Madsen G.J., Parker Q.A., 2006a, *Proc. IAU Symp.*, 234, 395
- Frew D.J., Parker Q.A., Russeil D., 2006b, *MNRAS*, 372, 1081
- Frew D.J., Bojičić I.S., Parker Q.A., 2012, *Proc. IAU Symp.*, 283, 362
- Frew D.J., Bojičić I.S., Parker Q.A., 2013a, *MNRAS*, in press, arXiv:1211.2505 (FBP13)
- Frew D.J. et al., 2013b, *MNRAS*, submitted (arXiv:1301.3994)
- Gaustad J.E., McCullough P.R., Rosing W., Van Buren D., 2001, *PASP*, 113, 1326
- Girart J.M., Viti S., 2007, *A&A*, 470, 633
- Goudis C., Meaburn J., 1978, *A&A*, 68, 189
- Gvaramadze V.V., Bomans D.J., 2008, *A&A*, 490, 1071
- Gvaramadze V.V., Kniazev A.Y., Fabrika S., 2010, *MNRAS*, 405, 1047
- Haffner L.M., Reynolds R.J., Tufte S.L., Madsen G.J., Jaehnig K.P., Percival J.W., 2003, *ApJS*, 149, 405
- Haffner L.M. et al., 2010, *ASPC*, 438, 388
- Hambly N.C., Miller L., MacGillivray H.T., Herd J.T., Cormack W.A., 1998, *MNRAS*, 298, 897
- Hambly N.C. et al., 2001, *MNRAS*, 326, 1279
- Hopewell E.C. et al., 2005, *MNRAS*, 363, 857
- Hutsemekers D., 1994, *A&A*, 281, L81
- Hutsemekers D., van Drom E., 1991, *A&A*, 251, 620
- Hua C.T., Dopita M.A., Martinis J., 1998, *A&AS*, 133, 361
- Jacoby G.H., Van de Steene G., 2004, *A&A*, 419, 563
- Jacoby G.H. et al., 2010, *PASA*, 27, 156
- Kerber F., Roth M., Manchado A., Gröbner H., 1998, *A&AS*, 130, 501
- Kistiakowsky V., Helfand D.J., 1993, *AJ*, 105, 2199
- Kovacevic A.V., Parker Q.A., Jacoby G.H., Sharp R., Miszalski B., Frew D.J., 2011, *MNRAS*, 414, 860
- Kronberger M. et al., 2012, *IAUS*, 283, 414
- MacGillivray H.T., Stobie R.S., 1984, *Vistas in Astronomy*, 27, 433
- Mader S.L., Zealey W.J., Parker, Q.A., Masheder M.R.W., 1999, *MNRAS*, 310, 331
- Madsen G.J., Reynolds R.J., Haffner L.M., 2006a, *ApJ*, 652, 401
- Madsen G.J., Frew D.J., Parker Q.A., Reynolds R.J., Haffner L.M., 2006b, *Proc. IAU Symp.*, 234, 455
- Mampaso A. et al., 2006, *A&A*, 458, 203
- Meaburn J., 1980, *MNRAS*, 192, 365
- Meaburn J., White N.J., 1982, *MNRAS*, 200, 771
- Miszalski B., Parker Q.A., Acker A., Birkby J.L., Frew D.J., Kovacevic A., 2008, *MNRAS*, 384, 525
- Miszalski B., Acker A., Parker Q.A., Moffat A.F.J., 2009, *A&A*, 505, 249
- Miszalski B., Boffin H.M.J., Frew D.J., Acker A., Köppen J., Moffat A.F.J., Parker Q.A., 2012, *MNRAS*, 419, 39
- Morgan D.H., Parker Q.A., 2005, *MNRAS*, 360, 360
- Morgan D.H., Parker Q.A., Cohen M., 2003, *MNRAS*, 346, 719
- Morgan D.H., Parker Q.A., Philipps S., 1999, *Proc. IAU Symp.*, 190, 95
- Muller E., Parker Q.A., 2007, *PASA*, 24, 69
- Murphy T., Cohen M., Ekers R.D., Green A.J., Wark R.M., Moss V., 2010, *MNRAS*, 405, 1560
- Nossal S., Roesler F.L., Bishop J., Reynolds R.J., Haffner M., Tufte S., Percival J., Mierkiewicz E.J., 2001, *JGR*, 106, 5605
- Nota, A., Livio M., Clampin M., Schulte-Ladbeck R., 1995, *ApJ*, 448, 788
- Parker Q.A., Bland-Hawthorn J., 1998, *PASA*, 15, 33

- Parker Q.A., Phillipps S., 1998, *PASA*, 15, 28
- Parker Q.A., Malin D., 1999, *PASA*, 16, 288
- Parker Q.A. et al., 2005, *MNRAS*, 362, 689 (Paper I)
- Parker Q.A. et al., 2006, *MNRAS*, 373, 79
- Parker Q.A., Frew D.J., Miszalski B., Kovacevic A.V., Frinchaboy P.M., Dobbie P.D., Köppen J., 2011, *MNRAS*, 413, 1835
- Parker Q.A., Frew D.J., Acker A., Miszalski B., 2012a, *Proc. IAU Symp.*, 283, 9
- Parker Q.A. et al., 2012b, *MNRAS*, 427, 3016
- Peimbert M., 1978, *Proc. IAU Symp.*, 76, 215
- Peimbert M., Rayo J.F., Torres-Peimbert S., 1975, *RMxAA*, 1, 289
- Perinotto M., Corradi R.L.M. 1998, *A&A*, 332, 721
- Pierce M.J., 2005, PhD thesis, University of Bristol
- Pierce M.J., Frew D.J., Parker Q.A., Köppen J., 2004, *PASA*, 21, 334
- Pinheiro M.C., Copetti M.V.F., Oliveira V.A., 2010, *A&A*, 521, 26
- Pollacco D., 1999, *MNRAS*, 304, 127
- Pretorius M.L., Knigge C., 2008, *MNRAS*, 385, 1471
- Reid I.N. et al., 1991, *PASP*, 103, 661
- Reid W.A., Parker Q.A., 2006a, *MNRAS*, 365, 401
- Reid W.A., Parker Q.A., 2006b, *MNRAS*, 373, 521
- Reid W.A., Parker Q.A., 2012, *MNRAS*, 425, 355
- Robbins W.J., Gaensler B.M., Murphy T., Reeves S., Green A.J., 2012, *MNRAS*, 419, 2623
- Ruffle P.M.E., Zijlstra A.A., Walsh J.R., Gray M.D., Gesicki K., Minniti D., Comeron F., 2004, *MNRAS*, 353, 796
- Ruiz M.T., 1983, *ApJ*, 268, L103
- Russeil D., Adami C., Amram P., Le Coarer E., Georgelin Y.M., Marcelin M., Parker Q., 2005, *A&A*, 429, 497
- Russeil D., Zavagno A., Motte F., Schneider N., Bontemps S., Walsh A.J., 2010, *A&A*, 515, A55
- Sabin L., Zijlstra A.A., Wareing C., Corradi R.L.M., Mampaso A., Viironen K., Wright N.J., Parker Q.A., 2010, *PASA*, 27, 166
- Shaw R.A., Kaler J.B., 1989, *ApJS*, 69, 495 (SK89)
- Smith A.G., Hoag A.A., 1979, *ARA&A*, 17, 43
- Stahl O., 1986, *A&A*, 164, 321
- Stahl O., 1987, *A&A*, 182, 229
- Stock D.J., Barlow M.J., 2010, *MNRAS*, 409, 1429
- Stock D.J., Barlow M.J., Wesson, R., 2011, *MNRAS*, 418, 2532
- Stupar M., Parker Q.A., 2009, *MNRAS*, 394, 1791
- Stupar M., Parker Q.A., 2011, *MNRAS*, 414, 2282
- Stupar M., Parker Q.A., 2012, *MNRAS*, 419, 1413
- Stupar M., Parker Q.A., Filipović M.D., 2007a, *MNRAS*, 374, 1441
- Stupar M., Parker Q.A., Filipović M.D., Frew D.J., Bojčić I., Aschenbach B., 2007b, *MNRAS*, 381, 377
- Stupar M., Parker Q.A., Filipović M.D., 2008, *MNRAS*, 390, 1037
- Tackenberg J., Beuther H., Plume R., Henning T., Stil J., Walmsley M., Schuller F., Schmiedeke A., 2013, *A&A*, 550, A116
- Tajitsu A., Tamura S., Yadoumaru Y., Weinberger R., Köppen J., 1999, *PASP*, 111, 1157
- Tritton S.B., 1983, *UKSTU Handbook*, Publication of the Royal Observatory, Edinburgh
- Tylenda R., Siódmiak N., Górny S.K., Corradi R.L.M., Schwarz H.E., 2003, *A&A*, 405, 627
- Urquhart J.S., Thompson M.A., Morgan L.K., Pestalozzi M.R., White G.J., Muna D.N., 2007, *A&A*, 467, 1125
- Viironen K. et al., 2009, *A&A*, 504, 291
- Viironen K. et al., 2011, *A&A*, 530, A107
- Wareing C.J., 2010, *PASA*, 27, 220
- Walker A.J., Zealey W.J., Parker Q.A., 2001, *PASA*, 18, 259
- Weinberger R., Kerber F., Gröbner H., 1997, *A&A*, 323, 963
- Xilouris K.M., Papamastorakis J., Sokolov N., Paleologou E., Reich W., 1994, *A&A*, 290, 639
- Xilouris K.M., Papamastorakis J., Paleologou E., Terzian Y., 1996, *A&A*, 310, 603
- Zavagno A., Pomarès M., Deharveng L., Hosokawa T., Russeil D., Caplan J., 2007, *A&A*, 472, 835